

# Solution landscapes of nematic liquid crystals confined on a hexagon

Yucen Han<sup>1</sup>, Jianyuan Yin<sup>2</sup>, Pingwen Zhang<sup>2</sup>, Apala Majumdar<sup>3</sup>, and Lei Zhang<sup>4</sup>

<sup>1</sup>*Beijing International Center for Mathematical Research, Peking University, Beijing 100871, China.*

<sup>2</sup>*School of Mathematical Sciences, Laboratory of Mathematics and Applied Mathematics, Peking University, Beijing 100871, China.*

<sup>3</sup>*Department of Mathematics and Statistics, University of Strathclyde, Glasgow, G1 1XH, United Kingdom.*

<sup>4</sup>*Beijing International Center for Mathematical Research, Center for Quantitative Biology, Peking University, Beijing 100871, China.*

We investigate the solution landscapes of a reduced Landau–de Gennes model for nematic liquid crystals on a two-dimensional hexagon at a fixed temperature, as a function of  $\lambda$ —the edge length. This is a generic example for reduced approaches on regular polygons. We apply the high-index optimization-based shrinking dimer method to systematically construct the solution landscape consisting of multiple defect solutions and relationships between them. We report a new stable T state with index-0 that has an interior  $-1/2$  defect; new classes of high-index saddle points with multiple interior defects referred to as H class and TD class; changes in the Morse index of saddle points with  $\lambda^2$  and novel pathways mediated by high-index saddle points that can control and steer dynamical pathways. The range of topological degrees, locations and multiplicity of defects offered by these saddle points can be used to navigate through complex solution landscapes of nematic liquid crystalline and other related soft matter systems.

## I. INTRODUCTION

Nematic liquid crystals (NLCs) are viscoelastic anisotropic material intermediate that combine the fluidity of liquids with the orientational order of solids [1]. The electro-optic properties of NLCs make them the working materials of choice for the multi-billion dollar liquid crystal display (LCD) industry. NLCs have tremendous potential in nanoscience, biophysics and material design, all of which rely on modeling and computational methods for studying stable/unstable NLC states, switching mechanisms, dynamical processes on energy landscapes etc. [2]. These approaches are useful for soft matter systems in general, for the study of interfacial phenomena, active matter, polymers, etc. [3–6]. A particularly intriguing feature of NLCs is topological defects, which are discontinuities in nematic directors or the averaged special directions of orientational ordering [1]. Defects commonly exist as isolated points or disclination lines in experiments [7]. Defects play important roles in physical phenomena, e.g. multistability in confinement, switching processes, self-assembly processes, materials design with defects as binding sites and colloid science [8, 9].

NLCs in confinement typically have multiple stable states that are critical points of an appropriately-defined free energy. The energy landscape of the NLC system is determined by the material properties, temperature, size and shape of the domain, boundary effects and external fields. In particular, the Landau–de Gennes (LdG) theory has been extensively applied in recent years to investigate the energy landscape of NLCs in confinement [8, 10–12], and there has been substantial analytic progress for the study of energy minima in confinement [13–16].

The confined NLC system can switch between different stable states by means of an external field, thermal fluctuations, noise and mechanical perturbations. The switching requires the system to cross an energy barrier through a transition state. The transition state is an index-1 saddle point, i.e., a critical point where the corresponding Hessian of the free energy has one and only one negative eigenvalue [17]. The transition state has the highest energy along the transition pathway that connects two neighbouring stable states. The reader is referred to [18] for transition pathways on a square domain with tangent boundary conditions and to [19] for transition pathways on a cylindrical domain with homeotropic boundary conditions.

There is substantial recent interest in high-index saddle points of the LdG free energy, which are critical points of the free energy, and the Morse index is the number of negative eigenvalues of the corresponding Hessian of the free energy [20]. For example, minimizing critical points have index 0 and transition states are index-1 saddle points. In recent years, powerful numerical algorithms have been developed to find multiple solutions of nonlinear equations, including the minimax method [21], the deflation technique [22], the eigenvector-following method [23], and the homotopy method [24, 25]. Despite substantial progress in this direction, the relationships between different solutions are unclear. In a recent work [26], Yin *et al.* propose a general numerical method that constructs the pathway map of NLCs confined in a square box—on a square domain. A hierarchy of connected solutions is identified on a square domain with tangent boundary conditions, including high-index saddle points. For small nano-scale square domains, it is known that the well ordered-reconstruction solution (WORS) with isotropic diagonals is the unique solution and the global energy minimum in this asymptotic regime [27, 28]. As the size of the square domain increases, WORS loses stability and its Morse index increases. Using WORS as the parent state (the highest-index saddle) and the high-

index optimization-based shrinking dimer (HiOSD) method, the authors construct a solution landscape on the square domain [26] and report novel saddle point solutions with multiple interior defects, that were previously unreported in the literature. This construction also offers multiple transition pathways (determined by the choice of the connecting saddle points) connecting the stable diagonal and rotated solutions for large square domains.

In this paper, we apply a reduced LdG model to numerically compute the complex solution landscapes of NLCs confined on a regular two-dimensional (2D) hexagonal domain with tangent boundary conditions. The reduced LdG model is suitable for 2D domains [29] and effectively reduces to the Ginzburg–Landau model for superconductors at a fixed temperature, which is representative of temperatures below the NLC supercooling temperature [30]. In this reduced approach, we only have two parameters—the topological degree of the tangent boundary conditions and the domain size  $\lambda^2$ . We largely vary  $\lambda$  and exploit the topological degree to some extent, to construct a hierarchy of critical points of the reduced LdG free energy on the hexagonal domain. The hierarchy includes the previously reported Ring, para (P) and meta (M) solutions in [31], which are distinguished by the locations, degrees and multiplicities of their defects. Furthermore, we find entirely new classes of high-index saddle points, e.g. the TD class (including index-6 saddle points) and the H-class (including an index-14 saddle point). The parent state on a hexagon changes from the Ring solution, to the T135 saddle point, and to the index-14 H-type saddle point as  $\lambda$  increases. It is noteworthy that we find a new type of index-0 stable solution with an interior  $-1/2$  defect, referred to as the T solution. We also observe certain numerical trends on how the vertex profile (bend-like versus splay-like) affects the Morse index as does the symmetry group of the saddle point. A plethora of saddle point solutions gives us diverse possibilities for transition pathways and indeed, we illustrate the differences between transition pathways with transition states or index-1 saddle points and transition pathways with high-index saddle points, e.g. two stable T solutions can be connected by an index-8 H-type saddle point. Some pairs of stable solutions are incompatible with transition states; they cannot be connected by a single transition state, e.g. two stable T solutions or indeed two different solutions in the P class, and this can be used to either impede or enhance switching for tailor-made applications.

There are deep analytic issues associated with saddle points of nonlinear and non-convex functionals, such as the reduced LdG free energy. We speculate that the LdG saddle points can be interpreted as minimizers of constrained problems or appropriately defined Dirichlet problems, as the WORS in [28]. Advances in this direction would lead to new control strategies for confined NLC systems, since we could propose conditions that would stabilise the saddle point solutions, some of which have multiple interior and boundary defects. Secondly, the hexagon is a generic regular polygon with an even number of sides. Our numerical results, at least from qualitative aspects, will carry over to arbitrary regular polygons with an even number of sides, and indeed to a large number of phase field models on 2D polygons with planar boundary conditions. Our results are indeed a consequence of the symmetry of the domain and the mathematical formulation, and as such, reveal certain universal trends of complex solution landscapes with regards to geometry, confinement and defects.

In Section II, we briefly review the reduced LdG framework for NLCs on 2D domains. In Section III, we review the HiOSD method for computing index- $k$  saddle points to construct the solution landscape. In Section IV, we systematically construct the solution landscapes with increasing complexity for  $\lambda^2 = 70, 120$  and  $600$  respectively, where the parameter  $\lambda^2$  is a measure of the hexagonal domain size. In Section V, we compare the solution landscapes on square and hexagon domains and we present our conclusions and perspectives in Section VI.

## II. LANDAU–DE GENNES THEORY

As a powerful continuum theory for NLCs, the Landau–de Gennes (LdG) theory describes the NLC state by a macroscopic order parameter—the  $\mathbf{Q}$ -tensor, which is a symmetric, traceless  $3 \times 3$  matrix [1]. The NLC is said to be in the isotropic phase if  $\mathbf{Q} = 0$ , uniaxial if  $\mathbf{Q}$  has a pair of repeated non-zero eigenvalues, and biaxial if  $\mathbf{Q}$  has three distinct eigenvalues. A uniaxial  $\mathbf{Q}$ -tensor is often written compactly as

$$\mathbf{Q} = s \left( \mathbf{n} \otimes \mathbf{n} - \frac{\mathbf{I}}{3} \right), \quad (1)$$

where  $\mathbf{n}$  is the nematic director or the eigenvector corresponding to the single eigenvalue that denotes the single distinguished direction of orientational ordering. We work with a particularly simple form of the LdG energy

$$I[\mathbf{Q}] := \int_{\Omega_\lambda} \frac{L}{2} |\nabla \mathbf{Q}|^2 + f_B(\mathbf{Q}) dA, \quad (2)$$

where  $\Omega_\lambda$  is a 2D hexagonal domain with edge lengths  $\lambda$ ,  $f_b$  is the bulk potential that drives the isotropic-nematic phase transition as a function of the temperature.

$$f_b = \frac{A}{2} \text{tr} \mathbf{Q}^2 - \frac{B}{3} \text{tr} \mathbf{Q}^3 + \frac{C}{4} \text{tr}(\mathbf{Q}^2)^2, \quad (3)$$

where  $B, C$  are positive material-dependent constants and  $A = \alpha(T - T^*)$  is the rescaled temperature. For  $A < 0$ ,  $f_b$  favours an ordered bulk uniaxial phase and the set of minimizers of  $f_b$  are uniaxial  $\mathbf{Q}$ -tensors (1), with

$$s = s_+ := \frac{B + \sqrt{B^2 + 24|A|C}}{4C}, \quad (4)$$

and arbitrary  $\mathbf{n} \in S^2$ . We non-dimensionalized the system with  $\bar{r} = r/\lambda$ , and the rescaled LdG energy functional is

$$\bar{I}[\bar{\mathbf{Q}}] := \int_{\Omega} \left[ \frac{1}{2} |\bar{\nabla} \bar{\mathbf{Q}}|^2 + \frac{\lambda^2}{L} f_b(\bar{\mathbf{Q}}) \right] d\bar{A}, \quad (5)$$

where  $\Omega$  is a regular polygon with unit edge lengths. In what follows, we drop the bars and all statements are in terms of the rescaled variables. The corresponding Euler-Lagrange equations are [32]:

$$\Delta \mathbf{Q} = \frac{\lambda^2}{L} \left( A \mathbf{Q} - B \left( \mathbf{Q} \mathbf{Q} - \frac{|\mathbf{Q}|^2}{3} \mathbf{I} \right) + C |\mathbf{Q}|^2 \mathbf{Q} \right). \quad (6)$$

The physically relevant states are modelled as local or global energy minima subject to the imposed boundary conditions.

In [29], the authors state that the physically relevant  $\mathbf{Q}$ -tensors on 2D domains have a fixed eigenvector  $\mathbf{z}$ , the unit vector in the  $z$ -direction, and can be written in terms of three variables  $q_1, q_2, q_3$  as shown below:

$$\mathbf{Q} = q_1 (\mathbf{n} \otimes \mathbf{n} - \mathbf{m} \otimes \mathbf{m}) + q_2 (\mathbf{n} \otimes \mathbf{m} + \mathbf{m} \otimes \mathbf{n}) + q_3 (2\mathbf{z} \otimes \mathbf{z} - \mathbf{n} \otimes \mathbf{n} - \mathbf{m} \otimes \mathbf{m}) \quad (7)$$

where  $\mathbf{n}$  and  $\mathbf{m}$  are orthonormal vectors in the  $xy$ -plane [29]. In other words, only three degrees of freedom out of five remains in a 2D framework. Further, in [32], the authors show that for  $A = -\frac{B^2}{3C}$ ,  $q_3$  is a constant  $\frac{-B}{6C}$  for all physically relevant solutions of (6) of the form (7), subject to Dirichlet uniaxial tangent boundary conditions on the domain edges. For a special temperature  $A = -\frac{B^2}{3C}$ ,  $q_3$  proves to be a constant for all physically relevant solutions of the form (7) to (6) with Dirichlet uniaxial tangent boundary conditions on the domain edges [32]. Hence, for  $A = -\frac{B^2}{3C}$ , we have a reduced description in terms of a reduced LdG tensor,  $\mathbf{P}$ , with only two degrees of freedom such that

$$\mathbf{Q} = \left( \begin{array}{c|c} \mathbf{P}(\mathbf{r}) + \frac{B}{6C} \mathbf{I}_2 & \begin{matrix} 0 \\ 0 \end{matrix} \\ \hline 0 & -B/3C \end{array} \right), \quad (8)$$

In what follows, we use the nodal set or the zero set of  $\mathbf{P}$  to track defects. The nodal set of  $\mathbf{P}$  is the set of uniaxial  $\mathbf{Q}$ -tensors with negative order parameter about  $\mathbf{z}$ , as can be seen above, which is consistent with disorder in the plane of  $\Omega$ .

$$E[\mathbf{P}] := \int_{\Omega} \left[ \frac{1}{2} |\nabla \mathbf{P}|^2 + \frac{\lambda^2}{L} \left( -\frac{B^2}{4C} \text{tr} \mathbf{P}^2 + \frac{C}{4} (\text{tr} \mathbf{P}^2)^2 \right) \right] dA. \quad (9)$$

Such reduced descriptions have been hugely successful for 2D systems or thin 3D systems, both for capturing the qualitative properties of physically relevant solutions and for probing into defect cores [33–37]. In a fully 3D system, there may be other classes of physically relevant solutions, such as escaped solutions, with additional degrees of freedom [19, 32] and this will be pursued in further work.

As illustrated in Figure 1, the regular hexagonal domain  $\Omega$  is centered at the origin with vertices

$$w_k = \left( \cos \frac{(k-1)\pi}{3}, \sin \frac{(k-1)\pi}{3} \right), \quad k = 1, \dots, 6.$$

Starting from  $(1, 0)$ , the edges are labeled counterclockwise as  $C_1, \dots, C_6$ , and the distance between a point on  $\partial\Omega$  and the vertex is defined as

$$\text{dist}(w) = \min\{\|w - w_k\|_2, k = 1, \dots, 6\}, \quad w \in \partial\Omega.$$

We work with the Dirichlet boundary condition  $\mathbf{P} = \mathbf{P}_b$  on the segments of edges, away from the vertices, defined to be

$$\begin{aligned} P_{11b}(w) &= \alpha_k = -\frac{B}{2C} \cos \left( \frac{(2k-1)2\pi}{6} \right), \quad \text{dist}(w) > \epsilon, w \text{ on } \partial\Omega, \\ P_{12b}(w) &= \beta_k = -\frac{B}{2C} \sin \left( \frac{(2k-1)2\pi}{6} \right), \quad \text{dist}(w) > \epsilon, w \text{ on } \partial\Omega, \end{aligned} \quad (10)$$

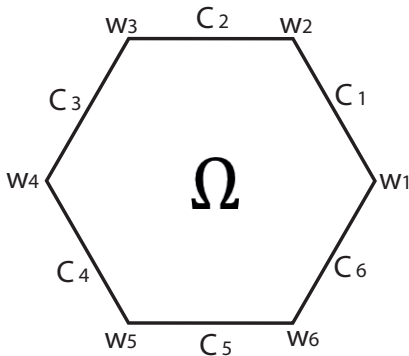


FIG. 1: hexagonal domain

where  $0 < \epsilon \ll 1/2$  is the size of mismatch region. We point out that  $\mathbf{P}_b \in \mathcal{N}$ . The value at the corner is the average of the two boundary conditions on the two intersecting edges.

The corresponding Euler-Lagrange equations for  $\mathbf{P}$  are

$$\begin{aligned} \Delta P_{11} &= \frac{2C\lambda^2}{L} \left( P_{11}^2 + P_{12}^2 - \frac{B^2}{4C^2} \right) P_{11}, \\ \Delta P_{12} &= \frac{2C\lambda^2}{L} \left( P_{11}^2 + P_{12}^2 - \frac{B^2}{4C^2} \right) P_{12}. \end{aligned} \quad (11)$$

We can also express  $\mathbf{P}$  in terms of an order parameter  $s$  and an angle  $\gamma$  as shown below:

$$\mathbf{P} = 2s \left( \mathbf{n} \otimes \mathbf{n} - \frac{1}{2} \mathbf{I}_2 \right), \quad (12)$$

where  $\mathbf{n} = (\cos \gamma, \sin \gamma)^T$  is the nematic director in the plane,  $s$  is a scalar order parameter that measures the degree of planar order about  $\mathbf{n}$  and  $\mathbf{I}_2$  is the  $2 \times 2$  identity matrix. Thus we have

$$P_{11} = s \cos(2\gamma), \quad P_{12} = s \sin(2\gamma).$$

In particular, one can use this representation to define the topological degree of  $\mathbf{P}_b$  above, i.e.,  $\gamma$  rotates by  $\pi k$ -radians around  $\partial\Omega$  for an integer  $k$  and the corresponding winding number of  $\mathbf{P}_b$  is  $k$  (with rotation of  $2\pi k$  around  $\partial\Omega$ ).

We define

$$\bar{\lambda}^2 = \frac{2C\lambda^2}{L},$$

the parameter in (11). We treat  $C, L$  to be fixed material-dependent constants, therefore  $\bar{\lambda}^2$  is proportional to  $\lambda^2$ . For brevity, we drop the bar over  $\lambda$  and use  $\lambda^2$  to represent  $\frac{2C\lambda^2}{L}$ , as a measure of the domain size.

### III. NUMERICAL METHOD

#### A. HiOSD method

As mentioned in the Introduction, it is a numerical challenge to find saddle point solutions, especially higher index saddle solutions, of nonlinear systems of partial differential equations such as the Euler-Lagrange equation in Eq. (11). In what follows, we employ the HiOSD method to efficiently compute the saddle points of any index, including minima which are saddle points of zero index, for the reduced LdG energy on a hexagon [38]. For a non-degenerate index- $k$  saddle point  $\hat{\mathbf{x}}$ , the Hessian  $\mathbb{H}(\hat{\mathbf{x}})$  has exactly  $k$  negative eigenvalues  $\hat{\lambda}_1 \leq \dots \leq \hat{\lambda}_k$  with corresponding unit eigenvectors  $\hat{\mathbf{v}}_1, \dots, \hat{\mathbf{v}}_k$  satisfying  $\langle \hat{\mathbf{v}}_j, \hat{\mathbf{v}}_i \rangle = \delta_{ij}$ ,  $1 \leq i, j \leq k$ . Define a  $k$ -dimensional subspace  $\hat{\mathcal{V}} = \text{span}\{\hat{\mathbf{v}}_1, \dots, \hat{\mathbf{v}}_k\}$ , then  $\hat{\mathbf{x}}$  is a local maximum on a  $k$ -dimensional linear manifold  $\hat{\mathbf{x}} + \hat{\mathcal{V}}$  and a local minimum on  $\hat{\mathbf{x}} + \hat{\mathcal{V}}^\perp$ , where  $\hat{\mathcal{V}}^\perp$  is the orthogonal complement space of  $\hat{\mathcal{V}}$ .

The HiOSD dynamics for a  $k$ -saddle ( $k$ -HiOSD) is given as follows [38]:

$$\begin{cases} \beta^{-1}\dot{\mathbf{x}} &= \left(\mathbf{I} - 2\sum_{j=1}^k \mathbf{v}_j \mathbf{v}_j^\top\right) (-\nabla E(\mathbf{x})), \\ \gamma^{-1}\dot{\mathbf{v}}_i &= -\left(\mathbf{I} - \mathbf{v}_i \mathbf{v}_i^\top - 2\sum_{j=1}^{i-1} \mathbf{v}_j \mathbf{v}_j^\top\right) \mathbb{H}(\mathbf{x})\mathbf{v}_i, \quad i = 1, \dots, k, \end{cases} \quad (13)$$

where the state variable  $\mathbf{x}$  and  $k$  direction variables  $\mathbf{v}_i$  are coupled,  $\mathbf{I}$  is the identity operator and  $\beta, \gamma > 0$  are relaxation parameters.

The first equation in (13) describes a transformed gradient flow, which allows  $\mathbf{x}$  to move along an ascent direction on the subspace  $\hat{\mathcal{V}}$  and a descent direction on the subspace  $\hat{\mathcal{V}}^\perp$ . The second equation in (13) is used to search for an orthonormal basis of  $\hat{\mathcal{V}}$ . Because the Hessian  $\mathbb{H}$  is self-adjoint in gradient systems, we can simply take  $\mathbf{v}_i$  to be a unit eigenvector corresponding to the  $i$ -th smallest eigenvalue of  $\mathbb{H}(\mathbf{x})$ . Thus, the  $i$ -th eigenvector  $\mathbf{v}_i$  can be obtained from a constrained optimization problem by using  $\mathbf{v}_1, \dots, \mathbf{v}_{i-1}$ , i.e.,

$$\min_{\mathbf{v}_i \in \mathbb{R}^n} \langle \mathbb{H}(\mathbf{x})\mathbf{v}_i, \mathbf{v}_i \rangle, \quad \text{s.t.} \quad \langle \mathbf{v}_j, \mathbf{v}_i \rangle = \delta_{ij}, \quad j = 1, 2, \dots, i. \quad (14)$$

Then we minimize the  $k$  Rayleigh quotients (14) simultaneously by solving the second equation in (13).

The  $k$ -HiOSD system (13) is coupled with an initial condition:

$$\mathbf{x}(0) = \mathbf{x}_0, \mathbf{v}_i(0) = \mathbf{v}_i^0, i = 1, \dots, k, \quad (15)$$

where  $\mathbf{x}_0 \in \mathbb{R}^n$ , and  $\{\mathbf{v}_1^0, \dots, \mathbf{v}_k^0\}$  are unit vectors in  $\mathbb{R}^n$  satisfying the orthonormal condition  $\langle \mathbf{v}_i^0, \mathbf{v}_j^0 \rangle = \delta_{ij}$ ,  $i, j = 1, 2, \dots, k$ .

To avoid direction-based calculation of Hessian, we use central difference schemes for directional derivatives to approximate the Hessian by  $k$  dimers centered at  $\mathbf{x}$ . The  $i$ th dimer ( $i = 1, \dots, k$ ) has a direction of  $\mathbf{v}_i$  with a small dimer length  $2l$  and  $\mathbb{H}(\mathbf{x})\mathbf{v}_i$  is approximated by

$$\mathbb{H}(\mathbf{x})\mathbf{v}_i = \frac{\nabla E(\mathbf{x} + l\mathbf{v}_i) - \nabla E(\mathbf{x} - l\mathbf{v}_i)}{2l}. \quad (16)$$

## B. Algorithm for constructing solution landscape

Solution landscape is a pathway map consisting of all stationary points and their connections [39]. Following the HiOSD dynamics, we construct the solution landscape by means of two algorithms: a downward search that enables us to search for all connected lower-index saddles from an index- $m$  saddle; an upward search with a selected direction to find the higher-index saddles, which drives the entire search to navigate up and down on the entire energy landscape [39].

*Downward search algorithm:* Given an index- $m$  saddle point  $\hat{\mathbf{x}}$  and  $m$  normalized vectors  $\hat{\mathbf{v}}_1, \dots, \hat{\mathbf{v}}_m$ , corresponding to the  $m$  negative eigenvalues  $\hat{\lambda}_1, \dots, \hat{\lambda}_m$  of the Hessian  $\mathbb{H}$ , we search for a lower index- $k$  ( $k < m$ ) saddle point using HiOSD dynamics (13). For the initial condition, we choose  $\mathbf{x}(0) = \hat{\mathbf{x}} \pm \epsilon \mathbf{u}$  for  $\mathbf{x}$ , where we perturb the high-index saddle  $\hat{\mathbf{x}}$  along  $\mathbf{u}$  direction with a small  $\epsilon$  to push the system away from the index- $m$  saddle. The direction  $\mathbf{u}$  is along a linear combination of  $(m - k)$  vectors in the set of unstable directions  $\{\hat{\mathbf{v}}_{k+1}, \dots, \hat{\mathbf{v}}_m\}$ , whose negative eigenvalues have the smallest magnitudes. The other  $k$  eigenvectors in the set  $\hat{\mathbf{v}}_1, \dots, \hat{\mathbf{v}}_k$  are used as the initial unstable directions  $\mathbf{v}_i(0)$ ,  $i = 1, \dots, k$ . A typical choice for  $k$ -HiOSD in a downward search is  $(\hat{\mathbf{x}} \pm \epsilon \hat{\mathbf{v}}_{k+1}, \hat{\mathbf{v}}_1, \dots, \hat{\mathbf{v}}_k)$ . Normally, a pair of index- $k$  saddles can be found, corresponding to the  $\pm$  sign in the initial guess. If the dynamics does not converge, then an index- $k$  saddle point does not exist starting from the initial search position  $\mathbf{x}(0)$  and initial direction  $\mathbf{v}_i(0)$ ,  $i = 1, \dots, k$ . A new initial condition is needed or another Morse index  $k$  is attempted.

*Upward search algorithm:* We can also search for a higher index- $k$  saddle from a index- $m$  saddle ( $m < k$ ) by using the HiOSD dynamics. The index- $m$  saddle is  $\hat{\mathbf{x}}$  with eigenvectors  $\hat{\mathbf{v}}_1, \dots, \hat{\mathbf{v}}_m$  corresponding to  $m$  negative eigenvalues. To search for a higher-index saddle, we need to calculate more directions  $\hat{\mathbf{v}}_{m+1}, \dots, \hat{\mathbf{v}}_k$ , which are eigenvectors corresponding to  $k - m$  smallest positive eigenvalues of  $\hat{\mathbf{x}}$ . For the initial condition  $\mathbf{x}(0) = \hat{\mathbf{x}} \pm \epsilon \mathbf{u}$ ,  $\mathbf{u}$  is a linear combination of  $(k - m)$  eigenvectors in the stable direction set  $\{\hat{\mathbf{v}}_{m+1}, \dots, \hat{\mathbf{v}}_k\}$ . A typical choice for  $k$ -HiOSD ( $k > m$ ) for an upward search is  $(\hat{\mathbf{x}} \pm \epsilon \hat{\mathbf{v}}_k, \hat{\mathbf{v}}_1, \dots, \hat{\mathbf{v}}_m, \hat{\mathbf{v}}_{m+1}, \dots, \hat{\mathbf{v}}_k)$ .

By repeating the downward search or upward search, we are able to systematically find saddle points of arbitrary index and uncover the connectivity of the complex solution landscape. In [31], the authors identify stable reduced equilibria in different regimes and use arc continuation methods to trace the corresponding solution branches. This method misses several solution branches, particularly disconnected branches and saddle point solutions. In the next sections, we use the HiOSD method to study the solution landscape for different values of  $\lambda$ , and as such, discover

new stable solutions, saddle point solutions e.g. TD and H solutions with multiple interior defects. Moreover, each downward or upward search represents a pseudo dynamics between different saddle points and this comprehensive numerical search also gives valuable insight into transition pathways between stable and unstable solutions, and the corresponding energy barriers.

### C. Spatial discretization on hexagon

The explicit square discretisation of domain is conventional. Here, to maintain the symmetry of hexagonal domain, we use finite difference schemes over hexagonal tessellations to estimate the spatial derivatives in the Laplacian [40]. The hexagonal domain is divided into regular hexagons with the spatial stepsize,  $h$ , and the variable of interest,  $\phi$  is measured at the center of each element. The 2D Laplacian operator is

$$\Delta = \frac{\partial^2}{\partial x^2} + \frac{\partial^2}{\partial y^2} = \frac{2}{3} \left( \frac{\partial^2}{\partial x_1^2} + \frac{\partial^2}{\partial x_2^2} + \frac{\partial^2}{\partial x_3^2} \right), \quad (17)$$

where  $x_1 = (1, 0)$ ,  $x_2 = (1/2, \sqrt{3}/2)$ ,  $x_3 = (-1/2, \sqrt{3}/2)$ . The approximation of  $\Delta\phi$  can be obtained from a Taylor expansion

$$\Delta\phi \approx \frac{(2/3)(\phi_E + \phi_{NE} + \phi_{NW} + \phi_W + \phi_{SW} + \phi_{SE}) - 4\phi_{j,k}}{h^2}, \quad (18)$$

where  $\phi_{j,k}$  represents the discrete value of the function  $\phi$  at coordinates  $(j, k)$ ,  $\phi_E$ ,  $\phi_{NE}$ ,  $\phi_{NW}$ ,  $\phi_W$ ,  $\phi_{SW}$ ,  $\phi_{SE}$  are values at the adjacent elements of  $(j, k)$  in east, north east, north west, west, south west, south east, respectively.

$$\left( \frac{\partial\phi}{\partial x} \right)^2 + \left( \frac{\partial\phi}{\partial y} \right)^2 = \frac{2}{3} \left( \left( \frac{\partial\phi}{\partial x_1} \right)^2 + \left( \frac{\partial\phi}{\partial x_2} \right)^2 + \left( \frac{\partial\phi}{\partial x_3} \right)^2 \right). \quad (19)$$

To calculate the elastic energy in (9), we approximate  $|\nabla\phi|^2$  as

$$|\nabla\phi|^2 \approx \frac{1}{3h^2} \left( (\phi_{j,k} - \phi_E)^2 + (\phi_{j,k} - \phi_{NE})^2 + (\phi_{j,k} - \phi_{NW})^2 + (\phi_{j,k} - \phi_W)^2 + (\phi_{j,k} - \phi_{SW})^2 + (\phi_{j,k} - \phi_{SE})^2 \right). \quad (20)$$

## IV. RESULTS

### A. Typical reduced solutions on the regular hexagon

We plot some typical reduced solutions on a 2D hexagon in Figure 2, all of which were reported in [31]. We impose Dirichlet uniaxial tangent boundary conditions on the hexagon edges, away from the vertices, which requires the leading eigenvector of  $\mathbf{P}$  (with the largest positive eigenvalue) to be in the plane of the hexagon and tangent to the edges. For small enough  $\lambda$ , we get the Ring solution with a +1 point defect at the centre, with a high degree of symmetry. The Ring solution exists for all  $\lambda$  and is globally stable in the reduced framework, in the  $\lambda \rightarrow 0$  limit [31]. The BD (boundary distortion) solution has two opposite +1/2 point defects near a pair of opposite edges, and this branch bifurcates from the Ring solution when the Ring solution loses stability as  $\lambda$  increases. There is an analogous bifurcation in a disc when the planar radial solution with a central +1 point defect bifurcates into planar polar solutions with two +1/2 point defects located along a diameter [41]. The Meta (M) solutions have two point defects at vertices separated by one vertex. The Para (P) are featured by a pair of diagonally opposite point defects and both the P and M solutions are stable for large enough  $\lambda$ . There are no interior defects in the M and P solutions. The stable Ortho (O) solutions, with two adjacent point defects at adjacent vertices, only exist for very large values of  $\lambda$  [31], and they will not be studied in this paper.

As  $\lambda$  increases, the solution landscape becomes increasingly complex. The defect core sizes are inversely proportional to  $\lambda^2$  and we obtain several saddle point solutions with interior point defects and vertex defects for large  $\lambda$ . Whilst it remains a challenge to find additional stable solutions, it seems that we can build a hierarchy of saddle point solutions with multiple critical points, that have defects of different topological degrees, with symmetric and asymmetric locations and the hierarchy may be further controlled by manipulating the topological degree of the Dirichlet boundary condition, whilst this is outside the scope of this paper.

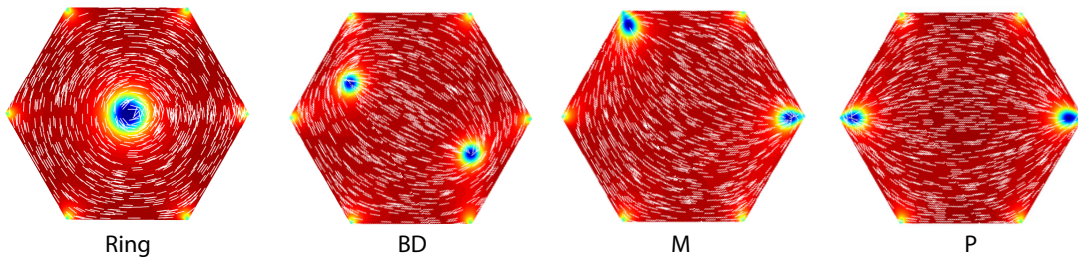


FIG. 2: Four typical solutions: Ring, BD, M, and P at  $\lambda^2 = 600$ .

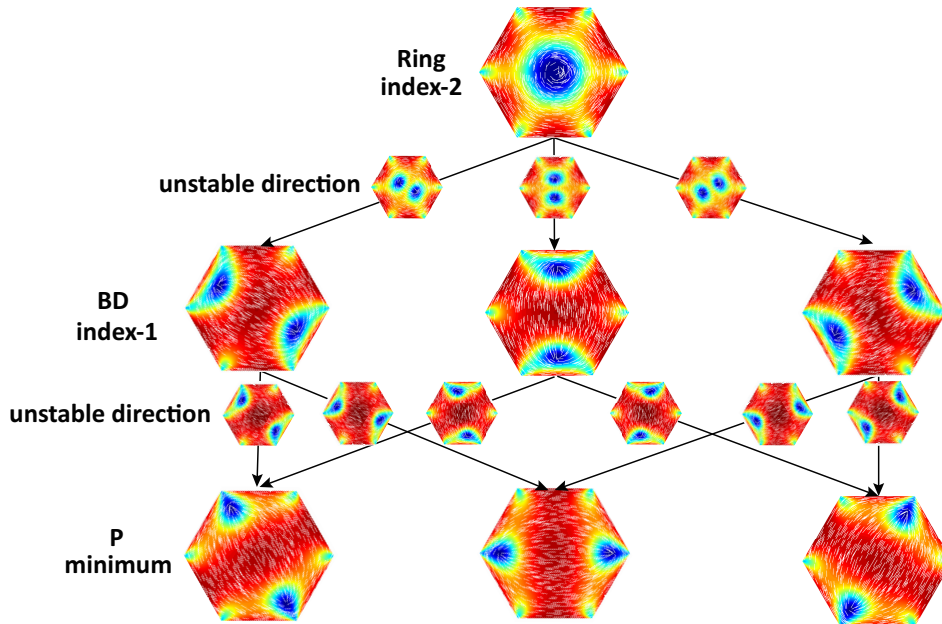


FIG. 3: Solution landscape at  $\lambda^2 = 70$ . Index-2 Ring is the parent state and connects to three index-1 BD solutions along its unstable directions. Each BD solution connects to two P minima along BD's single unstable direction. The color code is related to  $|\mathbf{P}|^2$  and the blue regions are defects. The white lines correspond to the planar nematic director without an arrow, since  $\mathbf{n} \equiv -\mathbf{n}$  for nematics.

### B. Solution landscape at $\lambda^2 = 70$

When  $\lambda^2$  is sufficiently small, the Ring solution is the unique stable solution [31]. We perform an increasing  $\lambda$  sweep for the Ring branch using Newton's method, the eigenvalues of the Ring solution monotonically decrease and we observe a pitchfork bifurcation at approximately  $\lambda^2 \approx 10$ , when we observe a transition from the unique stable Ring solution to multiple solutions [42]. For  $\lambda^2 \approx 10$ , the Ring solution transitions from zero index to a saddle point solution with index 2 (with two equal negative eigenvalues), and we additionally have index-1 BD solutions and index-0 P solutions. In general, we track bifurcations by tracking the indices of solutions; a change in the index is a signature of a bifurcation or change of stability properties. The solution landscape for  $\lambda^2 = 70$  is illustrated in Figure 3, showing the relationships between Ring, BD, and P solutions. Ring is the highest-index saddle as a parent state. Following each unstable eigen-direction of the Ring solution shown in Figure 3, the center +1 point defect splits into two defects that relax around a pair of opposite edges, i.e., the BD solutions. The two BD defects move from opposite edges to opposite vertices, following the unstable eigenvector of the BD solution and converging to the corresponding P solution.

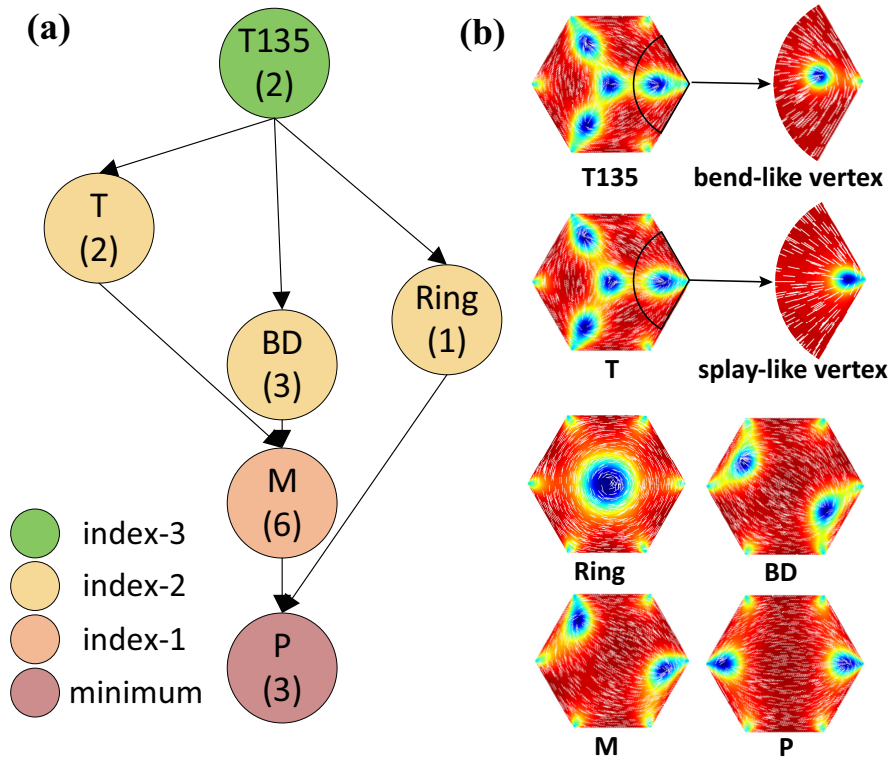


FIG. 4: (a) Solution landscape at  $\lambda^2 = 120$ . The colors of the node specify the Morse indices of saddle points. The number in the parentheses indicates the number of solutions without taking symmetry into account. The height of a node approximately corresponds to its energy in Eq. (13). (b) The six configurations of solutions in (a). A zoomed-in view of  $w_1$  for the T135 and T solutions with  $\lambda^2 = 600$ .

### C. Solution landscape at $\lambda^2 = 120$

We obtain new saddle points in Figure 4 for  $\lambda^2 = 120$ . The index-3 T135 replaces the index-2 Ring as a new parent state with two degenerate negative eigenvalues and one negative eigenvalue close to zero. The new index-2 T solution has two degenerate negative eigenvalues and we deduce that these two saddle point solutions emerge from a saddle-node bifurcation, i.e., they appear suddenly without connecting with other branches in the bifurcation diagram.

Both T and T135 solutions have a central  $-1/2$  point defect and three defects around alternate corners, with triangular symmetry. We can distinguish between the T and T135 solutions by zooming into the vertices (*bend-like vertex* or *splay-like vertex* in Figure 4(b)). For  $\lambda^2 = 600$ , we zoom into the  $w_1$  vertex to see the differences between T and T135 more clearly. In the T solution, the  $+1/3$  defect (around which the director  $\mathbf{n}$ , defined in (12), rotates by  $120^\circ$ ) is pinned to the vertex  $w_1$  and  $\mathbf{n}$  has a splay profile around  $w_1$ . We refer to such a vertex with a pinned defect as a *splay-like vertex*. In T135, the  $+1/3$  defect is split into a  $+1/2$  interior defect and a  $-1/6$  defect at  $w_1$  (around which  $\mathbf{n}$  exhibits a  $60^\circ$  rotation) with a high order intermediate region between the interior  $+1/2$  defect and  $w_1$ . We refer to  $w_1$  in T135 as a *bend-like vertex*. Regarding nomenclature, we use ‘T’ for triangular symmetry and the indices 135 label the bend-like vertices in T135. In T135, the bend-like vertices are located at  $w_1, w_3$  and  $w_5$  respectively. We deduce that solutions with bend-like vertices have a higher Morse index than those with splay-like vertices. The bend-like vertices have associated interior defects and we conjecture that this results in multiple unstable directions, and hence higher Morse index. The index-2 T solution has no bend-like vertices whereas the index-3 T135 solution has 3 bend-like vertices, more examples are given for the H and TD solutions in the next Section.

In comparison to  $\lambda^2 = 70$ , we also have new connections in Figure 4(a) from T135 to T, BD and Ring separately. The index-1 BD saddle solution bifurcates into an index-2 BD solution and an index-1 M saddle point. We have new connections between the BD, M and P solutions and the stable P solutions are connected by the index-1 M solutions in this case.

#### D. Solution landscape at $\lambda^2 = 600$

The solution landscape is quite complicated at  $\lambda^2 = 600$  in Figure 5(a). There are three notable numerical findings in this regime: a new stable T solution with an interior  $-1/2$  defect; new classes of saddle point solutions, H and TD, with high symmetry and high index and new saddle points with asymmetric defect locations. We recover the T135 as an index-3 saddle point; the index-2 T solution bifurcates into an index-0 T and an index-1 T0 and we also observe the new index-3 T130 solution and an index-2 solution, labelled by T10.

Regarding nomenclature, the 0 at the end of saddle point solutions T130, T10 and T0 indicates that the  $-1/2$  defect is displaced from the centre. The other numbers label the bend-like vertices as before. We illustrate these configurations in Figure 5(a) and Figure 5(b), and the number in parentheses is simply the number of such configurations related to each other by symmetry. The T135 and T solutions have three axes of reflection symmetry from the origin to  $w_1$ ,  $w_3$  and  $w_5$  respectively; T130 is symmetric with respect to reflections about the line connecting the origin to  $w_2$  and T0 is symmetric with respect to reflections about the line connecting the origin to the vertex  $w_3$ . The T10 saddle point has no axis of symmetry and there are 12 distinct T10 solutions, which are not related to each other by symmetry considerations.

The stable index-0 T solution is our first stable solution with an interior  $-1/2$  defect at the centre of the hexagon, for  $\lambda^2 > 250$ . The competing stable states, P and M, have defects pinned to vertices [31, 43], and these vertex defects are a natural consequence of the tangent boundary conditions and topological considerations (the total winding number of the boundary condition is zero). We speculate that there may be other stable solutions with interior point defects, particularly on polygons with a greater number of sides, since the disc has stable planar polar solutions with two interior  $+1/2$  defects. We also remark that the T solution on a hexagon for large  $\lambda$  is strongly reminiscent of the Ring solution on a regular triangle (Figure 5), as reported in [31], which suggests that we can build new solutions by tessellating solutions on simpler building block-type polygons, such as the triangle and the square.

In the next sections, we discuss saddle point solutions in the: H class (Figure 6) and TD class (Figure 7) that emerge from saddle-node bifurcations and pitchfork bifurcations with high Morse indices and multiple interior defects.

*Solution landscape of H class:* We numerically find a new class of saddle point solutions, labelled as H-class solutions, that have Morse indices ranging from 8 to 14. We plot the connectivity of these solutions in Figure 6(a), and the corresponding configurations and their defect profiles in Figure 6(b).

The parent state is the index-14  $H^*$  saddle point solution connecting to the lowest index-8 saddle point solution, labelled by H. Both of these states belong to the symmetry group  $G_6 := \{S \in O(2) : S\Omega \in \Omega\}$  (same as the Ring solution). Regarding nomenclature, we follow the same convention as before, i.e., H135 is an H-class saddle point with bend vertices at  $w_1, w_3, w_5$  respectively. The subscript \* labels the splay-like vertices (complement of bend-like vertices) so that  $H^*$  has no splay vertices whereas H has 6 splay vertices. Other examples include the index-13  $H1^*$  with one splay-like vertex  $w_1$  and the index-9  $H1$  solution has one bend-like vertex  $w_1$ ; the index-12  $H12^*$  has two splay-like vertices  $w_1$  and  $w_2$  and the index-10  $H12$  solution has two bend-like vertices at  $w_1$  and  $w_2$ ; the index-11  $H123$  solution has three bend-like vertices pinned at  $w_1, w_2$  and  $w_3$  respectively.

The H-saddle points look similar at first glance and we illustrate the subtle differences by plotting  $|\mathbf{P} - \mathbf{P}^H|$ , where  $\mathbf{P}$  is a solution of Eq. 11 in H-class and  $\mathbf{P}^H$  is the index-8 H solution. The differences concentrate at the vertices with conspicuous red or white points in the dark blue background (Figure 6(b)). These conspicuous points are localised near or at the bend-like vertices.

Numerically, we find that an index- $m$  solution in the H-class has  $(m - 8)$  bend-like vertices e.g. the index-8 H solution has no bend-like vertices whereas the index-14  $H^*$  solution has 6 bend-like vertices.

We follow the HiOSD dynamical process in Figure 6(c-d). In Figure 6(c), the unstable direction corresponding to the largest negative (most close to zero) eigenvalue of the H-saddle point drives the corresponding director,  $\mathbf{n}$  in (12), to rotate clockwise or anticlockwise. The  $-1/2$  interior point defect merges with one adjacent splay vertex defect and disappears to give a defect-free profile near the vertex. The spiral transient state finally converges to the Ring solution. In Figure 6(d), the unstable direction corresponding to the fifth largest negative eigenvalue of index-8 H saddle point, drives the three alternate  $-1/2$  defects in small triangles and  $+1$  defect in the center of hexagon to combine and annihilate, yielding a  $-1/2$  defect. The remaining alternate  $-1/2$  defects are pushed to the edges, the splay vertices disintegrate into bend-like vertices and from topological considerations, we are left with one central  $-1/2$  defect and three symmetrically placed interior  $+1/2$  defects. The final state is the T135 solution.

*Solution landscape of TD class:* We use TD as an abbreviation for “triangle double” since TD solutions appear to be a superposition of two Ring solutions on a regular triangle, with two interior  $-1/2$  point defects and an interior  $+1/2$  point defect. The lowest index saddle point solution in this class is the index-3 TD solution with no bend-like vertices. In general, a TD-type saddle point with  $m$  bend-like vertices is index- $(m + 3)$ , so that the highest index saddle point is  $TD^*$  with 3 bend vertices (the subscript \* has no vertex label attached to it which implies that there are no splay vertices). All saddle points in this class have three defective vertices, either bend-like or splay-like, as suggested by our numerical results and we illustrate the connectivity of this class in Figure 7(a). The TD class can

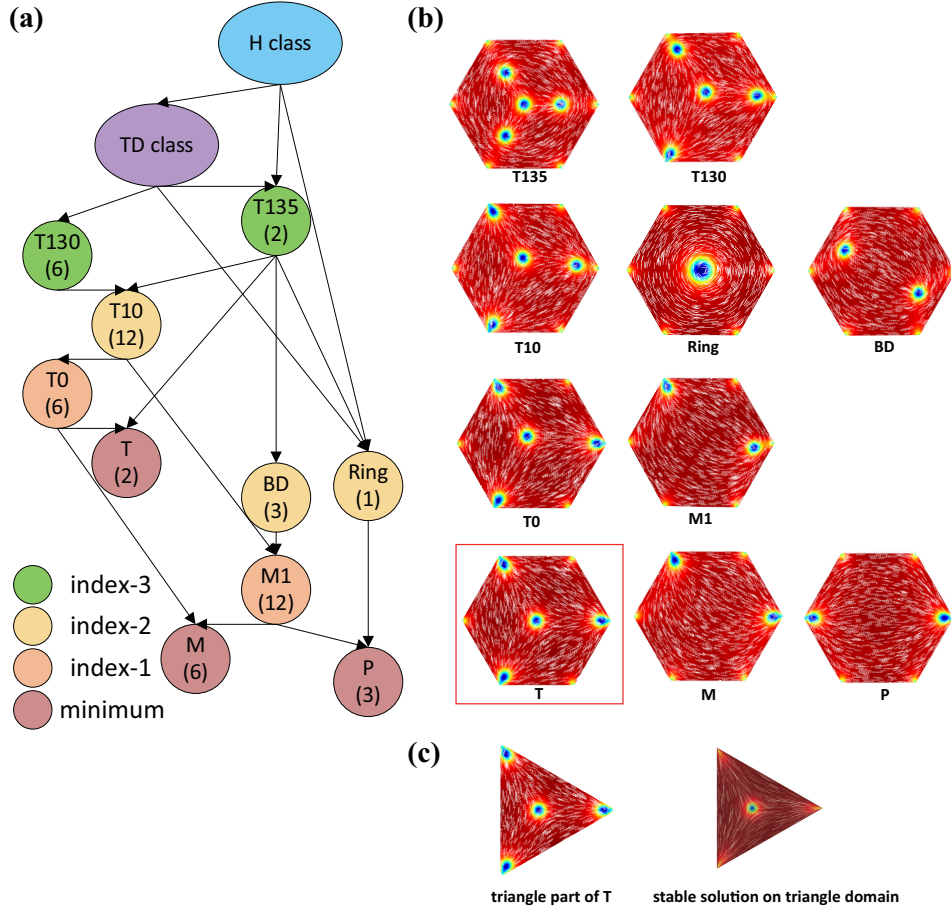


FIG. 5: (a) Solution landscape at  $\lambda^2 = 600$ . (b) The configurations correspond to (a). (c) The triangle part of T solution in hexagon domain  $\Omega$  and stable Ring solution on triangle domain with  $\lambda^2 = 450$ .

also be connected to the T130, Ring and T135 saddle points and these connections are displayed in Figure 5(a).

### E. Transition pathways between stable states

We illustrate a comprehensive network of transition pathways between stable states including two T, six M and three P solutions at  $\lambda^2 = 600$  in Figure 8. For convenience, we add subscripts to label the defect locations, since the hexagon is fixed and we need to cross energy barriers to switch between rotationally equivalent solutions (e.g. two different P or M solutions). In Figure 8, the T solution with defects pinned at  $w_2, w_4, w_6$  is labelled as  $T_{left}$  and the T solution with defects pinned at  $w_1, w_3, w_5$  is labelled as  $T_{right}$  respectively. The subscripts in  $T0_i$  simply identify the vertex closest to the displaced interior  $-1/2$  defect. We use the label M1 to identify a class of index-1 saddle points, configurationally close to the M solutions, with one splay-like vertex and one bend-like vertex. We use two subscripts, i.e.,  $M1_{a,b}$  to identify the location of the bend-like and splay-like vertices respectively. In contrast, the stable M and P solutions have two splay-like vertices and we use subscripts e.g.  $M_{a,b}$  to locate the splay-like vertices.

Firstly, we remark that some stable and configurationally-close solutions are connected by a single transition state (index-1 saddle point) in Figure 8. For example, the transition state between  $T_{left}$  and  $M_{26}$  is  $T0_4$ . The  $-1/2$  center point defect in  $T_{left}$  moves towards the vertex  $w_4$ , merges with the defect near  $w_4$  and the configuration converges to M. The transition state between  $M_{26}$  and  $P_{25}$  is  $M1_{62}$ . The defect at  $w_6$  moves towards  $w_5$  along the edge  $C_5$  between  $w_5$  and  $w_6$ , and settles at  $w_5$  yielding the stable  $P_{25}$  state.

Secondly, two different M or P solutions cannot be connected by means of a single transition state, i.e., the transition pathway is typically composed of at least two transition pathways with an intermediate M or P state. From a practical perspective, this means that there is a high probability for the system to be trapped into the intermediate stable M or P state. For instance, one transition pathway between  $P_{25}$  and  $P_{36}$  is  $P_{25}$ - $M1_{35}$ - $M_{35}$ - $M1_{53}$ - $P_{36}$ : The defect at  $w_2$

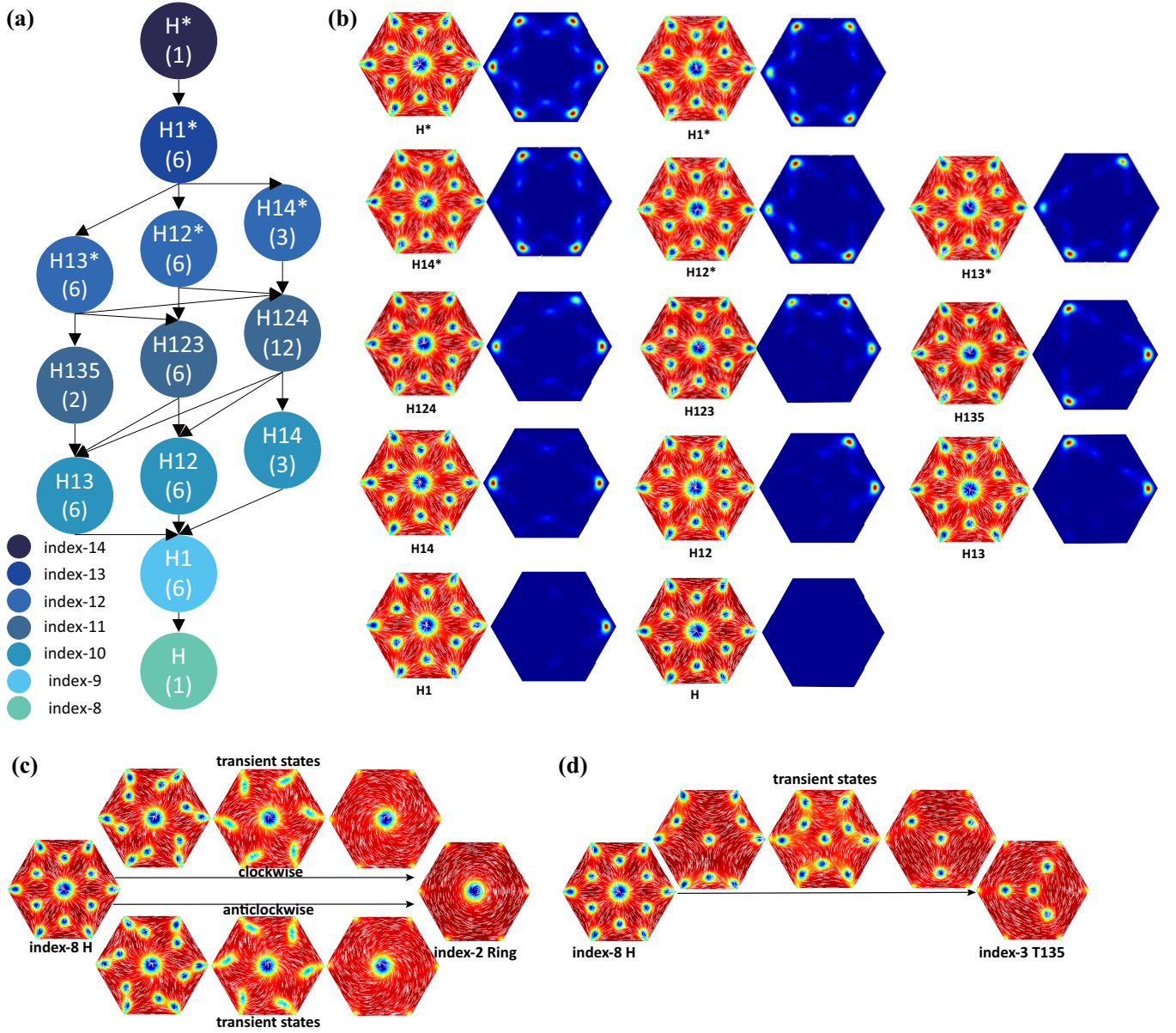


FIG. 6: (a) Solution landscape of H class. (b) The corresponding configurations and plots of  $|\mathbf{P} - \mathbf{P}^H|$ , where  $\mathbf{P}$  is any solution in H class,  $\mathbf{P}^H$  is index-8 H solution. (c) From index-8 H solution to index-2 Ring solution following the HiOSD dynamics in Eq. (13). (d) From index-8 H solution to index-3 T135 solution following the HiOSD dynamics in Eq. (13).

moves towards  $w_3$ , yielding the stable  $M_{35}$  and then the defect at  $w_5$  moves towards  $w_6$ , yielding the stable  $P_{36}$ .

Similarly, one transition pathway between  $M_{26}$  and  $M_{35}$  is  $M_{26}$ -  $M_{126}$ - $P_{36}$ - $M_{153}$ - $M_{35}$ , with an intermediate stable  $P_{36}$  state. The transient dynamics involves the migration of the defect at  $w_2$  towards  $w_3$ , which converges to  $P_{36}$ , followed by the motion of the defect at  $w_6$  towards the vertex  $w_5$  to yield the final stable state  $M_{35}$ .

The most complicated transition pathway appears to be the pathway between the two T solutions:  $T_{left}$  and  $T_{right}$ . Although  $T_{left}$  and  $T_{right}$  are two symmetric solutions related by a  $60^\circ$  rotation, the switching process between  $T_{left}$  and  $T_{right}$  cannot be achieved by a simple rotation because the hexagonal domain is fixed. In fact, one numerically computed transition pathway between  $T_{left}$  and  $T_{right}$  is  $T_{left}$ - $T_{04}$ - $M_{26}$ - $M_{162}$ - $P_{25}$ - $M_{115}$ - $M_{15}$ - $T_{03}$ - $T_{right}$ , where  $T_{04}$ ,  $M_{162}$ ,  $M_{115}$  and  $T_{03}$  are transition states or index-1 saddle points. This shows that a transition between two energetically degenerate but configurationally-far T solutions may have to overcome four energy barriers and could be easily trapped by the stable M or P solutions.

In Figure 8, each transition state can connect two stable minima by following its single unstable direction. This

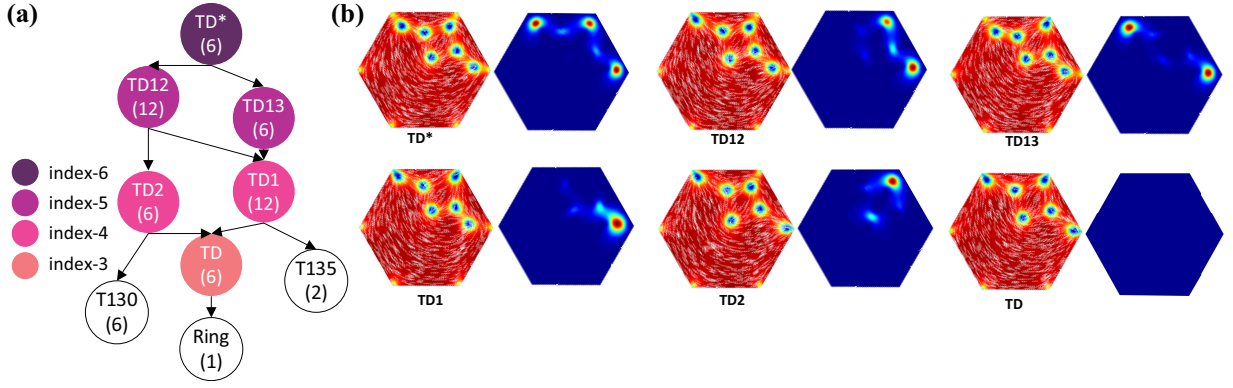


FIG. 7: (a) Solution landscape of TD class. (b) The corresponding configurations of TD class.

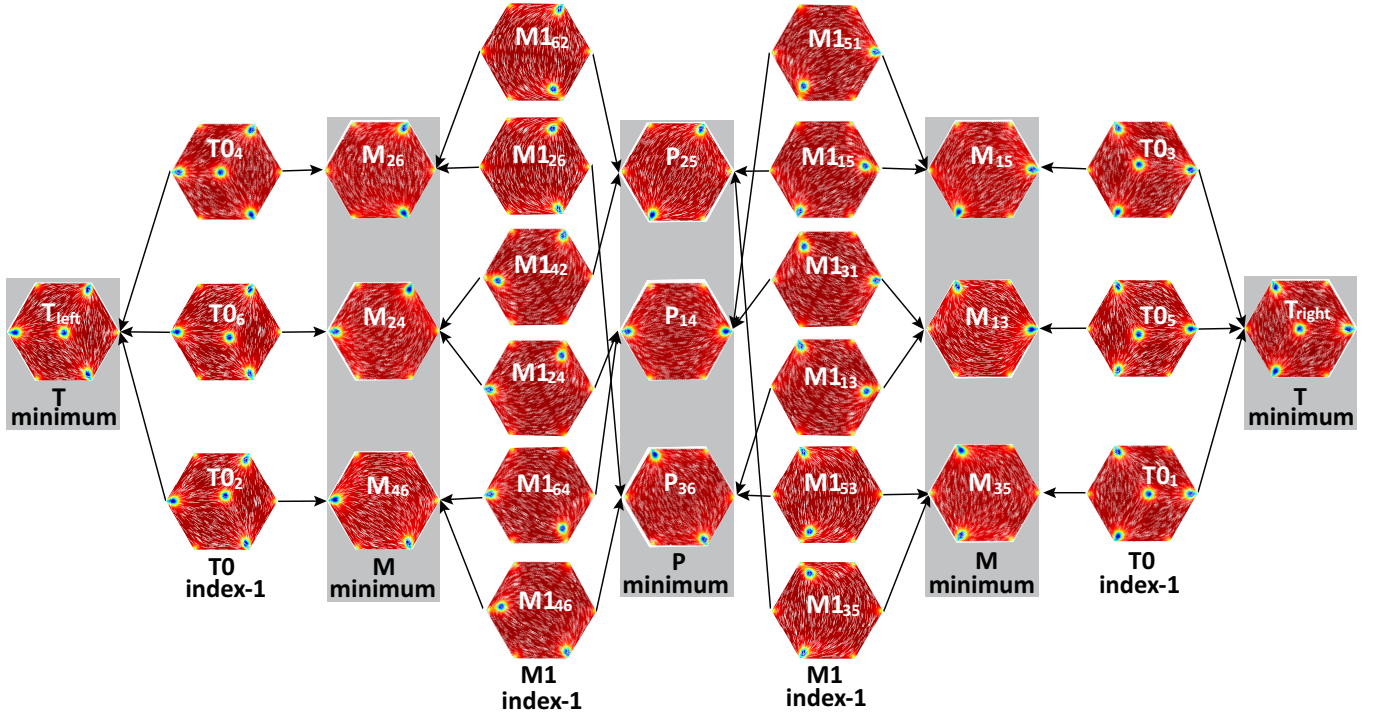


FIG. 8: The transition pathways between stable two T, six M and three P solutions with  $\lambda^2 = 600$ .

necessarily suggests that transition states cannot connect configurationally-far stable solutions, and hence multiple transition states are needed to connect configurationally-far stable states. This is computationally expensive and as suggested before, is not a reliable way of achieving switching because of the intermediate stable states. An alternative approach is to use higher-index saddle points with multiple unstable directions, to connect configurationally-far stable solutions. The multiple unstable directions give us greater control on the dynamical pathways and offer diverse possibilities, all of which give greater insight into the design and control of solution landscapes.

In Figure 9, we show how the different P, M, and T solutions are connected by high-index saddles. For instance, the index-1 M1 solutions connects the M and P solutions and the index-1 T0 solution connects the stable M and T solutions. However, two M solutions or two P solutions can be connected by the index-2 BD solution, e.g.  $M_{26} \leftarrow M_{162} \leftarrow BD_{25} \rightarrow M_{153} \rightarrow M_{35}$  and  $P_{25} \leftarrow M_{162} \leftarrow BD_{25} \rightarrow M_{153} \rightarrow P_{36}$ . The benefit of this pathway mediated by high-index saddle point as opposed to a pathway with an intermediate stable state is that the system will not be trapped by the transient unstable states along this pathway. Similarly, the M (P) solutions and T solutions are connected by the index-2 T10 solution as follows:  $T_{left} \leftarrow T_{04} \leftarrow T_{1042} \rightarrow M_{126} \rightarrow P_{36}$  or  $M_{26}$ .  $T_{left}$  and  $T_{right}$  solutions are configurationally far away

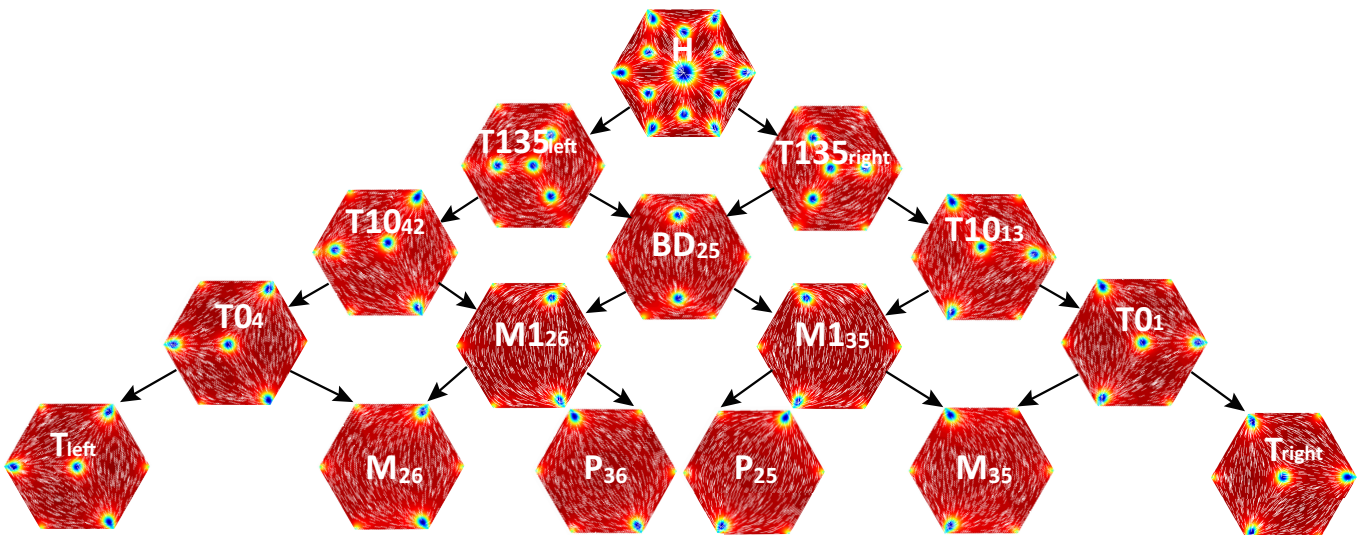


FIG. 9: Solution landscape starting from H solution. All local minima such as  $T_{left}$ ,  $P_{36}$ ,  $M_{26}$ ,  $M_{35}$ ,  $P_{25}$ , and  $T_{right}$  are connected by the index-8 H solution.

from each other and are thus connected by an index-8 H solution:  $T_{left} \leftarrow T_{135_{left}} \leftarrow H \rightarrow T_{135_{right}} \rightarrow T_{right}$ .

Figure 9 suggests that the index-8 H saddle point is connected to every stable solution and we can thus construct pathways between every pair of stable solutions. These pathways mediated by high-index saddle points typically have fewer steps and do not have intermediate index-0 states or stable states, and hence, can be more attractive and suitable for switching purposes in tunable NLC systems.

Our numerical results are not exhaustive but they do highlight the differences between transition pathways mediated by index-1 saddle points and pathways mediated by high-index saddle points. We deduce that index-1 saddle points are efficient for connecting configurationally-close stable solutions with a relatively low energy barrier. For configurationally-far stable states, we can construct transition pathways composed of transition states and intermediate stable states but these pathways have multiple steps and the system could easily be trapped in an intermediate state. A high-index saddle point would expedite the switching with fewer steps and no intermediate stable states, but we expect the energy barrier to be significantly higher. We plan to make quantitative studies on these lines in the future.

## V. COMPARISON WITH THE SOLUTION LANDSCAPE ON A SQUARE

The solution landscape of the LdG model has been systematically investigated on a square in [26]. This is a well-studied problem [27, 28] and it is known that the Well Order Reconstruction Solution (WORS) is the unique stable LdG equilibrium for small domain size, exists as a critical point for all domain size and is unstable for large domain size. The WORS is special in the sense that it is characterized by two isotropic defect lines along the square diagonals. In Figure 10 (a), the Morse index of the WORS increases with domain size and the WORS is always the parent state on a square. Intuitively, this is because the length of the diagonal defect lines increases as domain size increases, and thus the WORS has an increasing number of unstable directions and an increasing Morse index with increasing domain size. Whilst, the Ring solution on hexagon, the analogue of WORS, has dimension-0 point defect and maintains index-2 after bifurcation from index-0 Ring solution to index-2 Ring solution. The parent state with the highest index in the solution landscapes on a hexagon changes from Ring to index-3 T135 and index-14  $H^*$  when  $\lambda^2 = 70, 120, 600$  (Figure 10 (b)), where T135 and  $H^*$  solution emerge through saddle-node bifurcations. In the system confined on a hexagon, we have saddle-node bifurcations, stable solutions with interior point defects, and novel T, TD or H-type states which cannot be found for any numerically tested value of domain size on the square.

Although the solution landscapes on square and hexagon are different, we can find some analogous parts of the solution landscapes. The WORS and Ring are unique stable solutions when  $\lambda^2$  is small enough on square and hexagon, respectively. The BD on square or hexagon is the first unstable solution which bifurcates from WORS or Ring solutions. The D and R solutions are stable solutions on square [43] analogous to P and M solutions on hexagon when  $\lambda^2$  is large enough [31]. In the solution landscape on square,  $WORS \rightarrow BD \rightarrow D$  is analogous to  $Ring \rightarrow BD \rightarrow P$  on

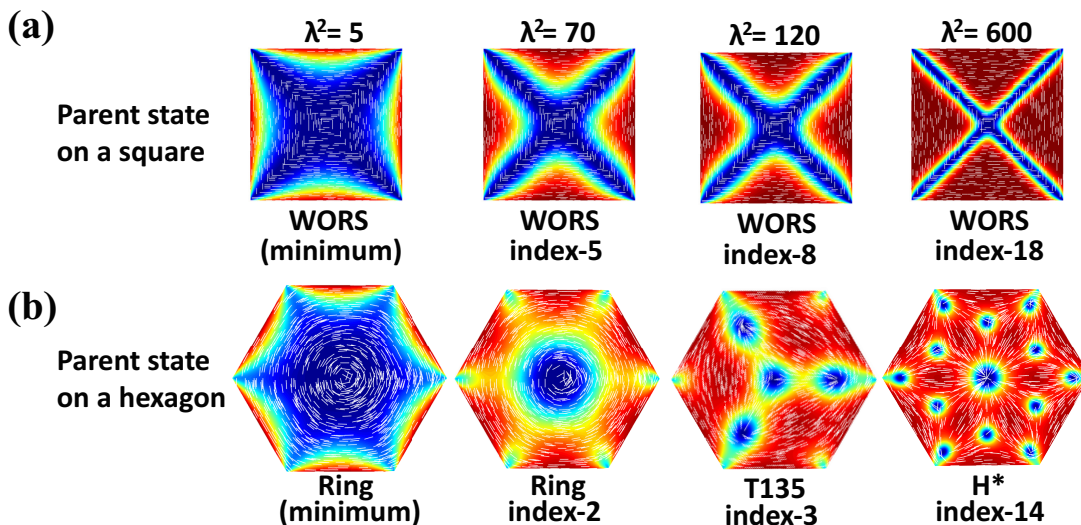


FIG. 10: Comparison of the parent states of the solution landscapes on square (a) and hexagon (b). The domain size  $\lambda^2 = 5, 70, 120$ , and  $600$ , respectively.

hexagon at  $\lambda^2 = 70$  in Figure 3. We believe that the hexagon is a more generic example of a regular polygon with an even number of sides than a square and hence, the qualitative properties of solution landscapes on a hexagon are expected to generalise to generic polygons with an even number of sides.

## VI. CONCLUSION

We study reduced LdG critical points on a regular 2D hexagon with tangent boundary conditions, as a prototype problem concerning nematic equilibria on regular 2D domains. We studied reduced LdG energy minima in [31], and we reported the Ring solution for nano-scale hexagons, and the P, M and O stable states for larger micron-scale hexagons, including a bifurcation diagram for the solution branches as a function of  $\lambda^2$ , i.e., we traced the continuation of these solution branches as a function of the hexagon size. We go much further in this manuscript in the sense that we focus on saddle points or unstable critical points that have a stable and unstable manifold respectively, i.e., they are unstable along a set of specified directions. We focus on saddle points of arbitrary Morse index, or arbitrary unstable directions; the most common saddle point is an index-1 saddle point with a single unstable direction, referred to as a transition state in the literature. We present illuminating numerical results on how the Morse index of solutions changes with  $\lambda$ , i.e., the Ring solution with a stable central +1-defect is index-0 for small  $\lambda$  and is index-2 for large  $\lambda$ . Similarly, the BD solution branch changes from index-1 to index-2 as  $\lambda$  increases. We believe this to be an interesting numerical result on how a given solution becomes more unstable as a function of the geometry. We observe new solution branches e.g. TD and H solutions through saddle-node bifurcations, and quite importantly, we report two new stable T solutions with a central  $-1/2$  defect, surrounded by three splay-like vertices. In fact, the T solution gains stability as  $\lambda$  increases, with a transition from index-2 to index-0 as  $\lambda$  increases, and is reminiscent of a the Ring solution for a regular triangle superimposed on a hexagonal domain [31]. This raises the pertinent question - can we construct reduced solutions on complex geometries by using reduced solutions on simpler geometries as a building block? We illustrate the solution landscapes at three representative values of  $\lambda^2$  and strongly speculate that there are more stable solutions, symmetric and asymmetric saddle point solutions, tessellated solutions as  $\lambda$  increases. Further, we have not exploited the topological degree of the boundary condition in our work, since the Dirichlet boundary conditions is either topologically trivial or has unit degree, in our simulations. We could build a further hierarchy of exotic reduced solutions by exploiting the topological degree of our tangent boundary condition.

A further innovative aspect of our work are insightful numerical results on dynamical pathways. We present several informative examples, of transition pathways with a single transition state, multiple transition states and pathways mediated by higher-index saddle points. We believe that pathways mediated by higher-index saddle points give greater possibilities for transition pathways, without the risk of being trapped into metastable states, and we can control the dynamical pathways by manipulating the different unstable directions. The selection mechanisms for dynamical pathways, in other words, how does a system choose between multiple dynamical pathways connecting a

pair of equilibria, remains an open problem of practical significance for liquid crystal devices.

We also remark that our results, though restricted to a 2D setting, will survive in a 3D setting too, for example on a well with a 2D hexagon as cross-section [32]. In fact, the Ring solution will survive as a translationally invariant solution on a 3D well, for arbitrary well heights, and will be globally stable for  $\lambda$  small enough, independently of well height. It is not clear if the Morse index of the saddle points will increase in a 3D setting and we expect this to be strongly dependent on the boundary conditions in a 3D setting.

The results in this paper pose several challenging analytic and numerical questions. Can we obtain bounds for the Morse index as a function of  $\lambda$ ? Is there an upper bound independent of  $\lambda$ , which would also impose restricting on the complexity of the solution landscape with increasing  $\lambda$ ? A reduced LdG tensor only has two degrees of freedom whereas the full LdG tensor in 3D has five degrees of freedom. We speculate that the T-solution on a hexagon may not be stable in a fully 3D framework. Other natural generalizations include the effects of asymmetry in the geometry, or the effects of elastic anisotropy and preliminary work shows that elastic anisotropy perturbs the symmetry of the problem, so that we may lose the Ring solution and the WORS with elastic anisotropy. Notably, we lose the structure of the Laplacian in the Euler-Lagrange equations which makes the problem analytically and computationally complex, with elastic anisotropy. We defer these investigations of the dimensionality, geometrical features and material anisotropy to future work.

**Acknowledgment** This work was supported by the National Natural Science Foundation of China No. 11861130351, 21790340, 11421101, and the Royal Society Newton Advanced Fellowship awarded to Lei Zhang and Apala Majumdar.

- 
- [1] Pierre Gilles de Gennes and J Prost. *The Physics of Liquid Crystals*, volume 83. Oxford university press, 1995.
  - [2] P. G. de Gennes and J. Prost. *The physics of liquid crystals*, volume 83. Oxford university press, 1995.
  - [3] L. Zhang, L. Q. Chen, and Q. Du. Morphology of critical nuclei in solid-state phase transformations. *Physical Review Letters*, 98(26):265703, 2007.
  - [4] Yucen Han, Zirui Xu, An-Chang Shi, and Lei Zhang. Pathways connecting two opposed bilayers with a fusion pore: a molecularly-informed phase field approach. *Soft Matter*, 2020.
  - [5] Teramoto Takashi and Nishiura Yasumasa. Morphological characterization of the diblock copolymer problem with topological computation. *Japan Journal of Industrial & Applied Mathematics*, 27(2):175–190, 2010.
  - [6] L. Zhang, W. Q. Ren, A. Samanta, and Q. Du. Recent developments in computational modelling of nucleation in phase transformations. *NPJ Computational Materials*, 2:16003, 2016.
  - [7] Oleg D Lavrentovich, Paolo Pasini, Claudio Zannoni, and Slobodan Zumer. *Defects in liquid crystals: Computer simulations, theory and experiments*, volume 43. Springer Science & Business Media, 2012.
  - [8] I. Muševič, M. Škarabot, U. Tkalec, M. Ravnik, and S. Žumer. Two-dimensional nematic colloidal crystals self-assembled by topological defects. *Science*, 313(5789):954–958, 2006.
  - [9] G. Foffano, J. S. Lintuvuori, A. Tiribocchi, and D. Marenduzzo. The dynamics of colloidal intrusions in liquid crystals: A simulation perspective. *Liquid Crystals Reviews*, 2(1):1–27, 2014.
  - [10] T. C. Lubensky, D. Petey, N. Currier, and H. Stark. Topological defects and interactions in nematic emulsions. *Physical Review E*, 57(1):610, 1998.
  - [11] L. Onsager. The effects of shape on the interaction of colloidal particles. *Annals of the New York Academy of Sciences*, 51(1):627–659, 1949.
  - [12] I. Bajc, F. Hecht, and S. Žumer. A mesh adaptivity scheme on the landau–de gennes functional minimization case in 3d, and its driving efficiency. *Journal of Computational Physics*, 321:981–996, 2016.
  - [13] Apala Majumdar and Yiwei Wang. Remarks on uniaxial solutions in the landau–de gennes theory. *Journal of Mathematical Analysis and Applications*, 464(1):328–353, 2018.
  - [14] Apala Majumdar and Arghir Zarnescu. Landau-de Gennes theory of nematic liquid crystals: the Oseen-Frank limit and beyond. *Archive for Rational Mechanics and Analysis*, 196(1):227–280, 2010.
  - [15] Duvan Henao, Apala Majumdar, and Adriano Pisante. Uniaxial versus biaxial character of nematic equilibria in three dimensions. *Calculus of Variations and Partial Differential Equations*, 56(2):55, 2017.
  - [16] Luc Nguyen and Arghir Zarnescu. Refined approximation for minimizers of a landau-de gennes energy functional. *Calculus of Variations and Partial Differential Equations*, 47(1-2):383–432, 2013.
  - [17] Lei Zhang, Qiang Du, and Zhenzhen Zheng. Optimization-based shrinking dimer method for finding transition states. *SIAM Journal on Scientific Computing*, 38(1):A528–A544, 2016.
  - [18] H. Kusumaatmaja and A. Majumdar. Free energy pathways of a multistable liquid crystal device. *Soft matter*, 11(24):4809–4817, 2015.
  - [19] Yucen Han, Yucheng Hu, Pingwen Zhang, and Lei Zhang. Transition pathways between defect patterns in confined nematic liquid crystals. *Journal of Computational Physics*, 396:1–11, 2019.
  - [20] John Willard Milnor, Michael Spivak, and Robert Wells. *Morse theory*, volume 1. Princeton university press Princeton, 1969.

- [21] Yongxin Li and Jianxin Zhou. A minimax method for finding multiple critical points and its applications to semilinear PDEs. *SIAM Journal on Scientific Computing*, 23(3):840–865, 2001.
- [22] P. E. Farrell, Á. Birkisson, and S. W. Funke. Deflation techniques for finding distinct solutions of nonlinear partial differential equations. *SIAM Journal on Scientific Computing*, 37(4):A2026–A2045, 2015.
- [23] Jonathan P. K. Doye and David J. Wales. Saddle points and dynamics of Lennard-Jones clusters, solids, and supercooled liquids. *The Journal of Chemical Physics*, 116(9):3777–3788, 2002.
- [24] Dhagash Mehta. Finding all the stationary points of a potential-energy landscape via numerical polynomial-homotopy-continuation method. *Physical Review E*, 84:025702, 2011.
- [25] Wenrui Hao, Jonathan D Hauenstein, Bei Hu, and Andrew J Sommese. A bootstrapping approach for computing multiple solutions of differential equations. *Journal of Computational and Applied Mathematics*, 258:181–190, 2014.
- [26] Jianyuan Yin, Yiwei Wang, Jeff Z. Y. Chen, Pingwen Zhang, and Lei Zhang. Construction of a pathway map on a complicated energy landscape. *Physical Review Letters*, 124:090601, 3 2020.
- [27] Samo Kralj and Apala Majumdar. Order reconstruction patterns in nematic liquid crystal wells. *Proceedings of the Royal Society A: Mathematical, Physical and Engineering Sciences*, 470(2169):20140276, 2014.
- [28] Giacomo Canevari, Apala Majumdar, and Amy Spicer. Order reconstruction for nematics on squares and hexagons: A Landau-de Gennes study. *SIAM Journal on Applied Mathematics*, 77(1):267–293, 2017.
- [29] Dmitry Golovaty, José Alberto Montero, and Peter Sternberg. Dimension reduction for the landau-de gennes model on curved nematic thin films. *Journal of Nonlinear Science*, 27(6):1905–1932, 2017.
- [30] Fabrice Bethuel, Haïm Brezis, Frédéric Hélein, et al. *Ginzburg-Landau Vortices*, volume 13. Springer, 1994.
- [31] Yucen Han, Apala Majumdar, and Lei Zhang. A reduced study for nematic equilibria on two-dimensional polygons. *arXiv preprint arXiv:1910.05740*, 2019.
- [32] Giacomo Canevari, Joseph Harris, Apala Majumdar, and Yiwei Wang. The well order reconstruction solution for three-dimensional wells, in the Landau-de Gennes theory. *arXiv preprint arXiv:1903.03873*, 2019.
- [33] A Brodin, A Nych, U Ognysta, B Lev, V Nazarenko, M Škarabot, and I Muševič. Melting of 2d liquid crystal colloidal structure. *Condensed Matter Physics*, 2010.
- [34] Apala Majumdar, Yiwei Wang, Banerjee Varsha, and Konark Bisht. Tailored morphologies in 2d ferronematic wells. *Europhysics Letters*, 2019.
- [35] Gaurav Gupta and Alejandro D Rey. Texture modeling in carbon-carbon composites based on mesophase precursor matrices. *Carbon*, 43(7):1400–1406, 2005.
- [36] Igor Musevic and Miha Škarabot. Self-assembly of nematic colloids. *Soft Matter*, 4(2):195–199, 2008.
- [37] Musevic Igor, Škarabot Miha, Tkalec Uros, Ravnik Miha, and Zumer Slobodan. Two-dimensional nematic colloidal crystals self-assembled by topological defects. *Science*, 313(5789):954–958, 2006.
- [38] Jianyuan Yin, Lei Zhang, and Pingwen Zhang. High-index optimization-based shrinking dimer method for finding high-index saddle points. *SIAM Journal on Scientific Computing*, 41(6):A3576–A3595, 2019.
- [39] Jianyuan Yin, Bing Yu, and Lei Zhang. Searching the solution landscape by generalized high-index saddle dynamics. *arXiv preprint arXiv:2002.10690*, 2020.
- [40] JC Fabero, Alfredo Bautista, and Luis Casasús. An explicit finite differences scheme over hexagonal tessellation. *Applied Mathematics Letters*, 14(5):593–598, 2001.
- [41] Yucheng Hu, Yang Qu, and Pingwen Zhang. On the disclination lines of nematic liquid crystals. *Communications in Computational Physics*, 19(2):354–379, 2016.
- [42] Hans Troger and Alois Steindl. *Nonlinear stability and bifurcation theory: an introduction for engineers and applied scientists*. Springer Science & Business Media, 2012.
- [43] Martin Robinson, Chong Luo, Patrick E Farrell, Radek Erban, and Apala Majumdar. From molecular to continuum modelling of bistable liquid crystal devices. *Liquid Crystals*, 44(14-15):2267–2284, 2017.